

Jiazhen Leng

Mem. ASME
Department of Mechanical Engineering,
McGill University,
817 Sherbrooke Street West,
Montreal, QC H3A 0C3, Canada
e-mail: jiazhen.leng@mcgill.ca

Gerard Reynolds

Department of Mechanical Engineering,
McGill University,
817 Sherbrooke Street West,
Montreal, QC H3A 0C3, Canada
e-mail: gerard.reynolds@mail.mcgill.ca

Megan Schaezner

Siemens Power and Gas,
9545 Côte-de-Liesse,
Dorval, QC H9P 1A5, Canada
e-mail: megan.schaezner@siemens.com

Minh Quan Pham

Siemens Power and Gas,
9545 Côte-de-Liesse,
Dorval, QC H9P 1A5, Canada
e-mail: minhquan.pham@siemens.com

Genevieve Bourgeois

Siemens Power and Gas,
9545 Côte-de-Liesse,
Dorval, QC H9P 1A5, Canada
e-mail: genevieve.bourgeois@siemens.com

Ali Shanian

Siemens Power and Gas,
9545 Côte-de-Liesse,
Dorval, QC H9P 1A5, Canada
e-mail: ali.shanian@siemens.com

Damiano Pasini¹

Mem. ASME
Department of Mechanical Engineering,
McGill University,
817 Sherbrooke Street West,
Montreal, QC H3A 0C3, Canada
e-mail: damiano.pasini@mcgill.ca

Stress Concentration in Low-Porosity Periodic Tessellations With Generic Patterns of Elliptical Holes Under Biaxial Strain

Stress concentration in porous materials is one of the most crucial culprits of mechanical failure. This paper focuses on planar porous materials with porosity less than 5%. We present a stress-prediction model of an arbitrarily rotated elliptical hole in a rhombus shaped representative volume element (RVE) that can represent a class of generic planar tessellations, including rectangular, triangular, hexagonal, Kagome, and other patterns. The theoretical model allows the determination of peak stress and distribution of stress generated near the edge of elliptical holes for any arbitrary tiling under displacement loading and periodic boundary conditions. The results show that the alignment of the void with the principal directions minimizes stress concentration. Numerical simulations support the theoretical findings and suggest the observations remain valid for porosity as large as 5%. This work provides a fundamental understanding of stress concentration in low-porosity planar materials with insight that not only complements classical theories on the subject but also provides a practical reference for material design in mechanical, aerospace, and other industry. [DOI: 10.1115/1.4040539]

1 Introduction

Architected materials can be designed to feature properties that exceed those of conventional solids, thus appealing a wide range of applications across disciplines [1]. Typical engineering applications where they have been applied so far for structural purposes include those requiring maximum stiffness for structural integrity [2–4], enhanced fatigue life [5], or maximum energy absorption under impact loading [6]. Other applications where their functional potential has been exploited focus on the design of tunable properties, such as negative Poisson's ratio [7–15], band gaps [16–20], heat transfer [21], negative or zero coefficient of thermal expansion [22–27], mechanical biocompatibility [28–31], and many others [1]. Architected materials are generally assembled

from building blocks tessellated in a two-dimensional or three-dimensional space, and such process can be employed in hierarchical arrangements [13,20,26,32,33]. The design method may be developed from intuition and rationalized [34], and the implementation of shape [23] and topology optimization [35] can explore the design space even further.

Despite the wealth of contributions in the area of porous architected materials, the majority examine high-porosity domains, typically larger than 70%, a choice that generally allows greater tunability. The performance of low porosity, e.g., 5–10%, architected materials has been less explored thus far. Recent works which examined ultralow porosity (<2%) domains with elliptical holes staggered in orthogonal tessellation, focused mainly on tailoring Poisson's ratio and band gaps [36,37]. In more recent work, emphasis has been placed on the shape of the hole, and an orthogonally tessellated “S” shaped slot was proposed, which showed enhanced fatigue life that outperforms traditional circular holes [38]. Besides ordered patterns of voids, randomly oriented slits

¹Corresponding author.

Manuscript received March 24, 2018; final manuscript received May 28, 2018; published online July 6, 2018. Assoc. Editor: Shaoxing Qu.

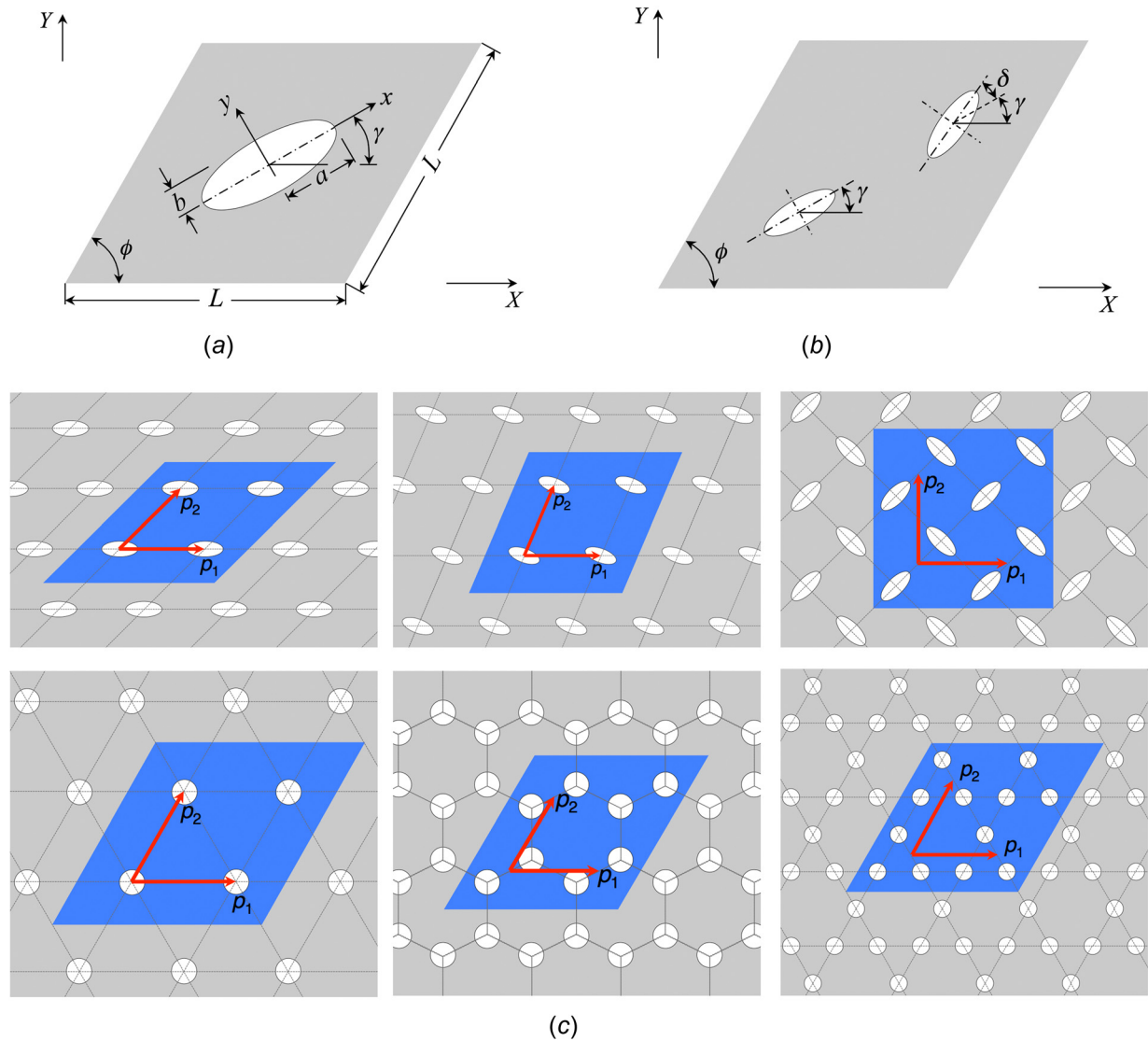


Fig. 1 Description of geometric variables and examples of tessellation: (a) RVE and geometric variables of one elliptical hole, (b) Rotation of two holes in the RVE, and (c) Void patterns with triangular, hexagonal, and Kagome tessellations

have been also studied in planar tessellations, and auxeticity has been shown to be possible in disordered arrangements [39]. Other related works on low-porosity metamaterials include those featuring orthogonal cuts of sinusoidal half-wave in their initial geometry, which under tension show bistable behavior followed by a pattern switch that creates a drastic increase of porosity [40]. Furthermore, orthogonally arranged cuts in thin sheets under tension have been proposed to generate spatial morphology induced by the out-of-plane plastic buckling of their ligaments [41]. Despite recent advances in low porosity planar tessellations, most of the literature has focused on normally arranged cuts or voids typically with one circular shape and constant orientation; the mechanics of tessellations that departs from the conditions of (i) orthogonality imposed to the periodic vectors, (ii) uniform orientation of the void, as well as (iii) unicity of the void in the representative volume element (RVE), remain unexplored so far.

The objective of this paper is to investigate stress concentration in arbitrary planar tessellations of elliptical holes with varying orientations and generically arranged vectors of periodicity in low-porosity domains. Stress concentration is a crucial and well-studied cause for mechanical failure. Stress concentration on the edge of holes started from the circular hole in an infinite domain under uniform tension [42,43] to a wide range of further development including other void geometries [43–48], semi-infinite or

finite domain [43,49,50], reinforcements [43,50,51], multiple holes [43,52,53], nonisotropic materials [43,54–57], and other load cases [43,56,58,59]. However, what has not been so far explored is the effect of tessellation type and periodic boundary conditions on stress distribution and peak stress. Section 2 of the paper examines the stress distribution and stress concentration near the edge of elliptical holes of generic tessellations and presents a theoretical model of stress prediction, which is used in Sec. 3 to search for the direction of the periodic vectors that can best mitigate the stress regime in any arbitrary tessellation. Prediction curves are also presented to capture the role of the aspect ratio of elliptical holes in various load cases. Numerical results in Sec. 4 verify theoretical observations and further discussion examines the threshold value of porosity below which the model presented here holds.

2 Theoretical Model for Representative Volume Element With Low Porosity

2.1 Assumptions and Theoretical Model of the Strain Field. We consider a periodic planar domain with low porosity in the range of 0% to 10–15%. The geometry of the void shape under investigation is illustrated in Fig. 1(a). The void shape is an

arbitrarily rotated ellipse with semiaxes a and b aligned to the local coordinate system xy . The ellipse can assume a rotation γ from the global Cartesian coordinate system XY . The elliptical void is centered in a generic rhombus RVE with edge length L and internal angle ϕ defining the orientation of the periodic vector of a given tessellation. We also examine an RVE with two holes of identical shape, which have a relative rotation of angle δ (see Figs. 1(a) and 1(b)) to each other. Since ϕ defines the orientation of the periodic vectors (arrows in Fig. 1(c)), a large family of tessellations can be described by the RVEs containing multiple holes. The second row in Fig. 1(c) shows some tessellation patterns (triangular, hexagonal, and Kagome) that can be generated with the adoption of a generic rhombus RVE of multiple holes. With this framework, the variables of interest are the aspect ratio a/b of the ellipse, the ellipse rotation angle γ , the relative rotation between holes, δ , and the angle ϕ between the periodic vectors.

The porosity in this study is defined as

$$\psi = \frac{A_{\text{Hole}}}{A_{\text{RVE}}} \quad (1)$$

For which the following assumptions hold:

- 1) The domain is periodic, unbounded, and subjected to uniform displacements along directions X and Y in the global Cartesian system. The mechanical behavior can be deduced by the study of the RVE under periodic boundary conditions.
- 2) Porosity is assumed below 5%, a value that enables the use of bulk properties for the solid making up the RVE. The validity of this assumption is examined in Sec. 4, where the deviation from the theoretical model is compared with that from the numerical analysis for increasing values of porosity.
- 3) Deformation of the RVE is small and the material behavior is linear elastic thus small strain theory can be applied in the theoretical model.

Figure 2 shows a rhombus RVE with marked edges and corners subjected to biaxial displacement. The horizontal edge is aligned with the global X direction. In two-dimensions, the periodic boundary conditions on the displacements are

$$\begin{aligned} u_R - u_L &= u_2 - u_1, & v_R - v_L &= v_2 - v_1 \text{ for left and right} \\ u_T - u_B &= u_4 - u_1, & v_T - v_B &= v_4 - v_1 \text{ for top and bottom} \end{aligned} \quad (2)$$

where the horizontal and vertical displacements $u(x, y)$ and $v(x, y)$ are functions defined at every material point (x, y) in the global coordinate system XY . Subscripts T, B, L, R denote the top, bottom, left, and right edges of the RVE and node numbers at its corners.

To eliminate rigid body motion and to account for the general case of the existence of shear strain in the RVE, the following set of four displacement conditions is applied at node 1, 2, and 4. This choice is necessary to capture nonzero shear strains emerging in an RVE tessellated at an angle other than 90 deg

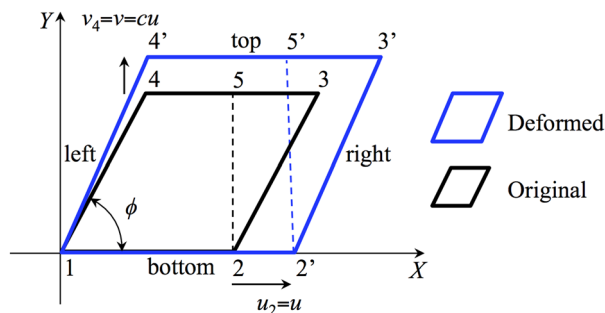


Fig. 2 Displacement loading and deformation pattern of the RVE

$$\begin{aligned} u_1 &= v_1 = 0 \\ v_2 &= 0 \\ u_4 &= 0 \end{aligned} \quad (3)$$

Uniform displacements u and $v = cu$ are applied to the right and top edges of the RVE. With enforced boundary conditions, the rhombus RVE deforms into a parallelogram; hence, the displacements of the four corners of the RVE are given by

$$\begin{aligned} u_1 &= v_1 = 0 \\ u_2 &= u, & v_2 &= 0 \\ u_3 &= u, & v_3 &= v = cu \\ u_4 &= 0, & v_4 &= v = cu \end{aligned} \quad (4)$$

Since point 5 has the y coordinate of point 3 and 4, and $u_4 = 0$ and $u_3 = u$, by linear scaling using distances from point 4 to point 5 and point 4 to point 3, we find the displacements of point 5

$$u_5 = u(1 - \cos \phi), \quad v_5 = v = cu \quad (5)$$

With $\phi \neq 0$, the resulting strain components of the RVE from the displacement field are

$$\begin{aligned} \epsilon_{xx} &= \frac{\partial u}{\partial x} = \frac{u}{L} \\ \epsilon_{yy} &= \frac{\partial v}{\partial y} = \frac{c}{\sin \phi} \epsilon_{xx} = c \frac{u}{L \sin \phi} \\ \gamma_{xy} &= \frac{\partial u}{\partial y} + \frac{\partial v}{\partial x} = \frac{\partial u}{\partial y} = \frac{u_5 - u_2}{L \sin \phi} = -\frac{u}{L} \cot \phi \end{aligned} \quad (6)$$

With $\epsilon_{xy} = \gamma_{xy}/2$, the solution of the eigenvalue problem yields the principal strains for $0 \text{ deg} < \phi \leq 90 \text{ deg}$

$$\begin{aligned} \epsilon_1 &= \frac{u(c + \sin \phi - \sqrt{c^2 - 2c \sin \phi + 1})}{2L \sin \phi} \\ \epsilon_2 &= \frac{u(c + \sin \phi + \sqrt{c^2 - 2c \sin \phi + 1})}{2L \sin \phi}, \quad \epsilon_1 < \epsilon_2 \end{aligned} \quad (7)$$

And, the corresponding principal directions are obtained by taking the inverse tangent function of the eigenvectors

$$\begin{aligned} v_1 &= \left[\frac{c - \sin \phi + \sqrt{c^2 - 2c \sin \phi + 1}}{\cos \phi}, 1 \right] \\ v_2 &= \left[\frac{c - \sin \phi - \sqrt{c^2 - 2c \sin \phi + 1}}{\cos \phi}, 1 \right] \end{aligned} \quad (8)$$

By evaluating the displacement ratio $c = -\nu \sin \phi$ with the bulk material's Poisson's ratio ν , uniaxial displacement loading (in the X direction) can be handled as a special case with the principal strains and principal directions given by

$$\begin{aligned} \epsilon_1 &= \frac{u(1 - \nu - \sqrt{\cot^2 \phi + \nu^2 + 2\nu + 1})}{2L} \\ \epsilon_2 &= \frac{u(1 - \nu + \sqrt{\cot^2 \phi + \nu^2 + 2\nu + 1})}{2L}, \quad \epsilon_1 < \epsilon_2 \end{aligned} \quad (9)$$

$$\begin{aligned} v_1 &= \left[-\frac{1 + \nu - \sqrt{\cot^2 \phi + \nu^2 + 2\nu + 1}}{\cot \phi}, 1 \right] \\ v_2 &= \left[-\frac{1 + \nu + \sqrt{\cot^2 \phi + \nu^2 + 2\nu + 1}}{\cot \phi}, 1 \right] \end{aligned} \quad (10)$$

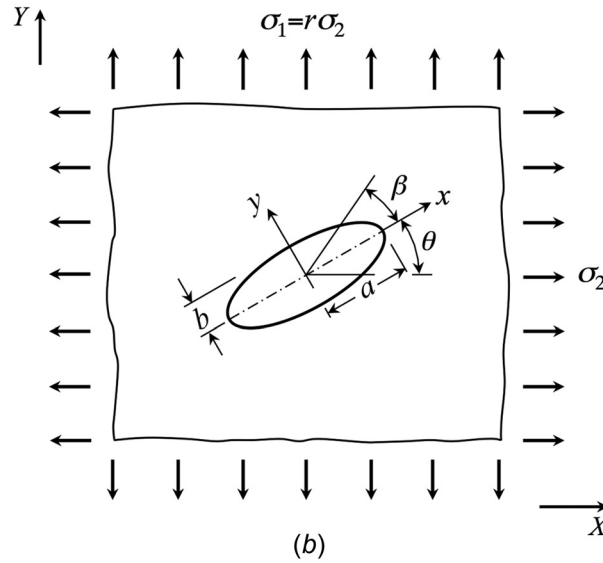
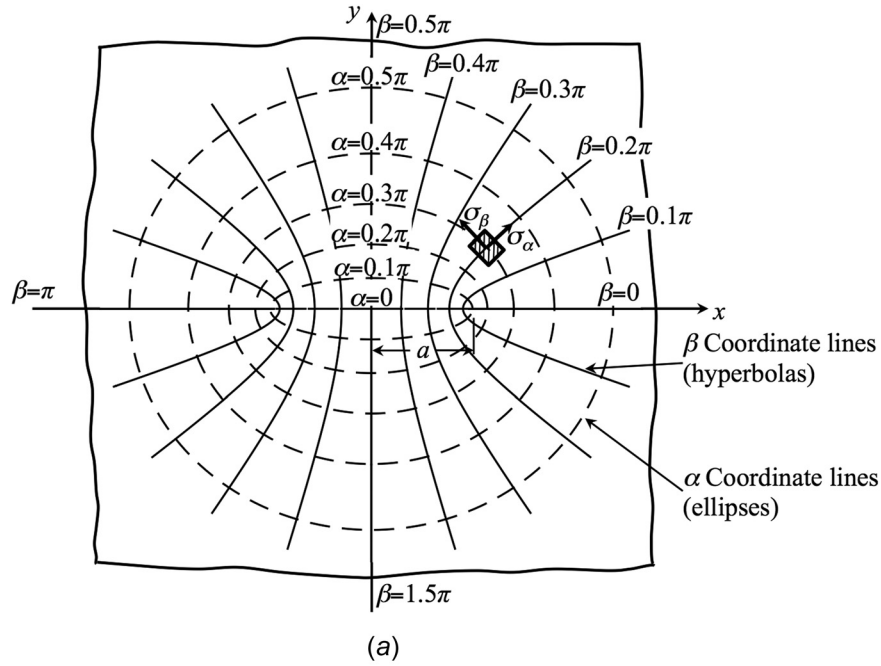


Fig. 3 Elliptical coordinate system and biaxial loading of the elliptical hole: (a) Illustration of the elliptical coordinate system, with constant coordinate curves of α and β and (b) Rotated elliptical hole under biaxial loading. σ_1 is linearly proportional to σ_2 by the factor r .

2.2 Theoretical Model of the Stress Field and Stress Distribution Around the Hole. Multiplication of the plane stress constitutive matrix of the linear elastic material with Young's modulus E and the principal strain vector yields the two principal stresses

$$\sigma_1 = -\frac{Eu \left[(1+\nu)(c + \sin \phi) - (1-\nu)\sqrt{c^2 - 2c \sin \phi + 1} \right]}{2L \sin \phi (\nu^2 - 1)}$$

$$\sigma_2 = -\frac{Eu \left[(1+\nu)(c + \sin \phi) + (1-\nu)\sqrt{c^2 - 2c \sin \phi + 1} \right]}{2L \sin \phi (\nu^2 - 1)} \quad (11)$$

For the special case of uniaxial loading, the principal stresses are

$$\sigma_1 = \frac{Eu \left(1 + \nu - \sqrt{\nu^2 + 2\nu + 1/\sin^2 \phi} \right)}{2L(1+\nu)}$$

$$\sigma_2 = \frac{Eu \left(1 + \nu + \sqrt{\nu^2 + 2\nu + 1/\sin^2 \phi} \right)}{2L(1+\nu)}, \quad \sigma_1 < \sigma_2 \quad (12)$$

With principal stresses, we can apply classical theory to determine the stress distribution near the edge of a tilted elliptical hole in an infinite domain [43,60]. We do so by using the elliptical coordinate system parameterized by α and β shown in Fig. 3(a). Here, the rotation θ is defined with respect to the principal direction of σ_2 (see Fig. 3(b)) and should not be confused with γ in Fig. 1, which is the global rotation of the hole with respect to the global X -direction. The closed form expression of the stress distribution is

$$(\sigma_\beta)_{\alpha_0} = \frac{(1+r)\sigma_2 \sin h 2\alpha_0 + (1-r)\sigma_2 [\cos 2\theta - e^{2\alpha_0} \cos 2(\beta - \theta)]}{\cos h 2\alpha_0 - \cos 2\beta},$$

$$(\sigma_\alpha)_{\alpha_0} = 0 \quad (13)$$

where $r = \sigma_1/\sigma_2$ and $\alpha_0 = \tanh^{-1}(b/a)$ [43,60]. It is assumed that σ_2 is larger in magnitude, and the principal stress ratio r ranges between -1 and 1 ; hence, covering the range of loading conditions that are of interest. Note that the stress component normal to the edge of the elliptical hole, σ_z , is always zero.

If the maximum stress is determined from Eq. (13), then dividing it by the reference stress yields the stress concentration factor as

$$K_t = \frac{\sigma_{\max}}{\sigma_{\text{ref}}} = \frac{\max(\sigma_\beta)}{\sigma_2} \quad (14)$$

where σ_{ref} is the reference stress in the definition of the stress concentration factor. In our case, it is the larger principal stress σ_2 .

3 Parametric Study of Stress Concentration

Equation (13) is now used to examine the effect of the rotation and aspect ratio of the elliptical hole for given stress ratio $r = \sigma_1/\sigma_2$ before extending the analysis to arbitrary tessellations.

3.1 Void Rotation. Symbolic forms of the aspect ratio a/b (represented by α_0), principal stress ratio r , and arbitrary rotation

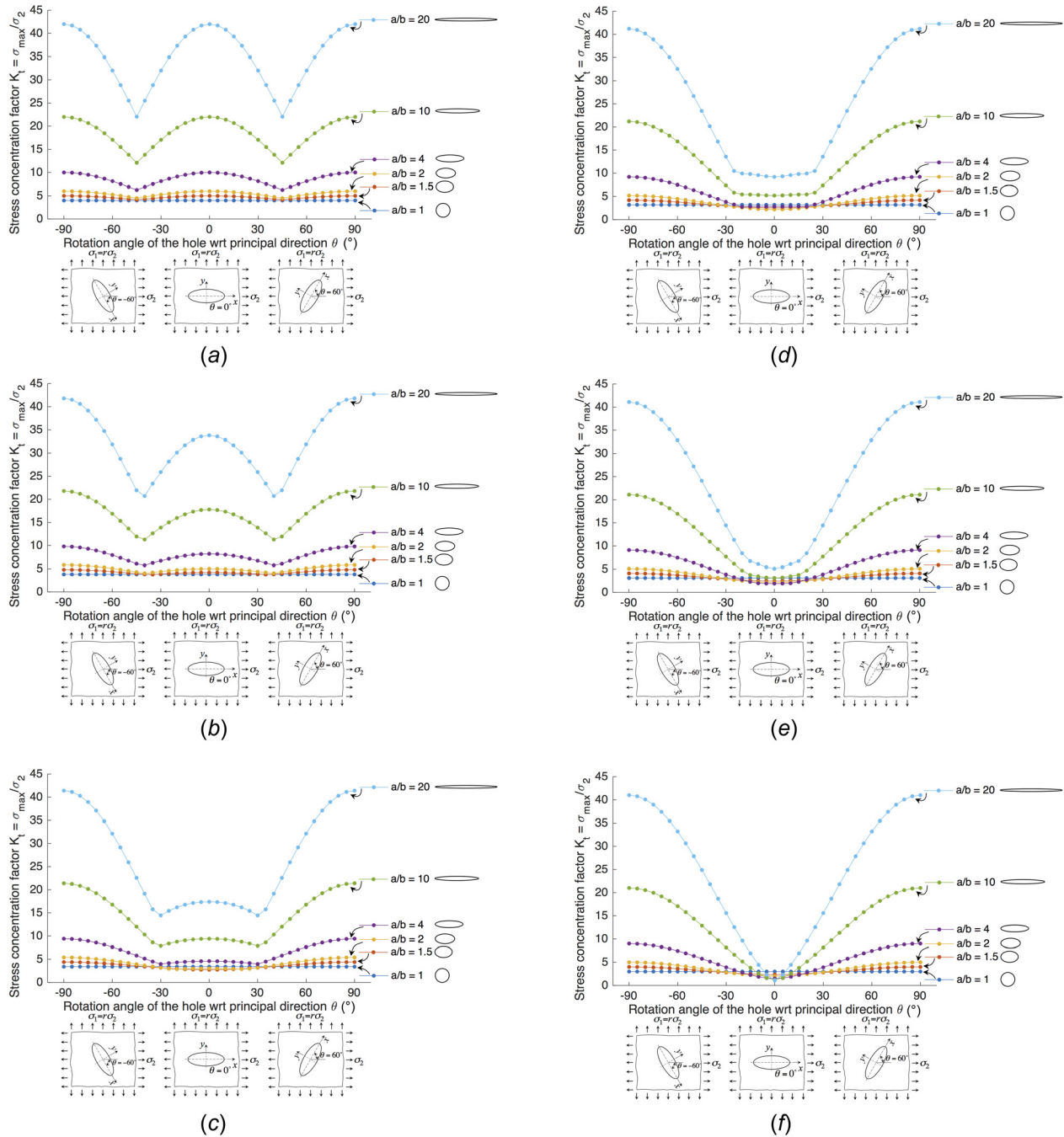


Fig. 4 Curves of stress concentration factor (K_t) versus θ for given a/b , parameterized by σ_1/σ_2 : (a) $\sigma_1/\sigma_2 = -1.0$, (b) $\sigma_1/\sigma_2 = -0.8$, (c) $\sigma_1/\sigma_2 = -0.4$, (d) $\sigma_1/\sigma_2 = -0.2$, (e) $\sigma_1/\sigma_2 = -0.1$, (f) $\sigma_1/\sigma_2 = 0$, (g) $\sigma_1/\sigma_2 = 0.1$, (h) $\sigma_1/\sigma_2 = 0.2$, (i) $\sigma_1/\sigma_2 = 0.4$, (j) $\sigma_1/\sigma_2 = 0.8$, and (k) $\sigma_1/\sigma_2 = 1.0$

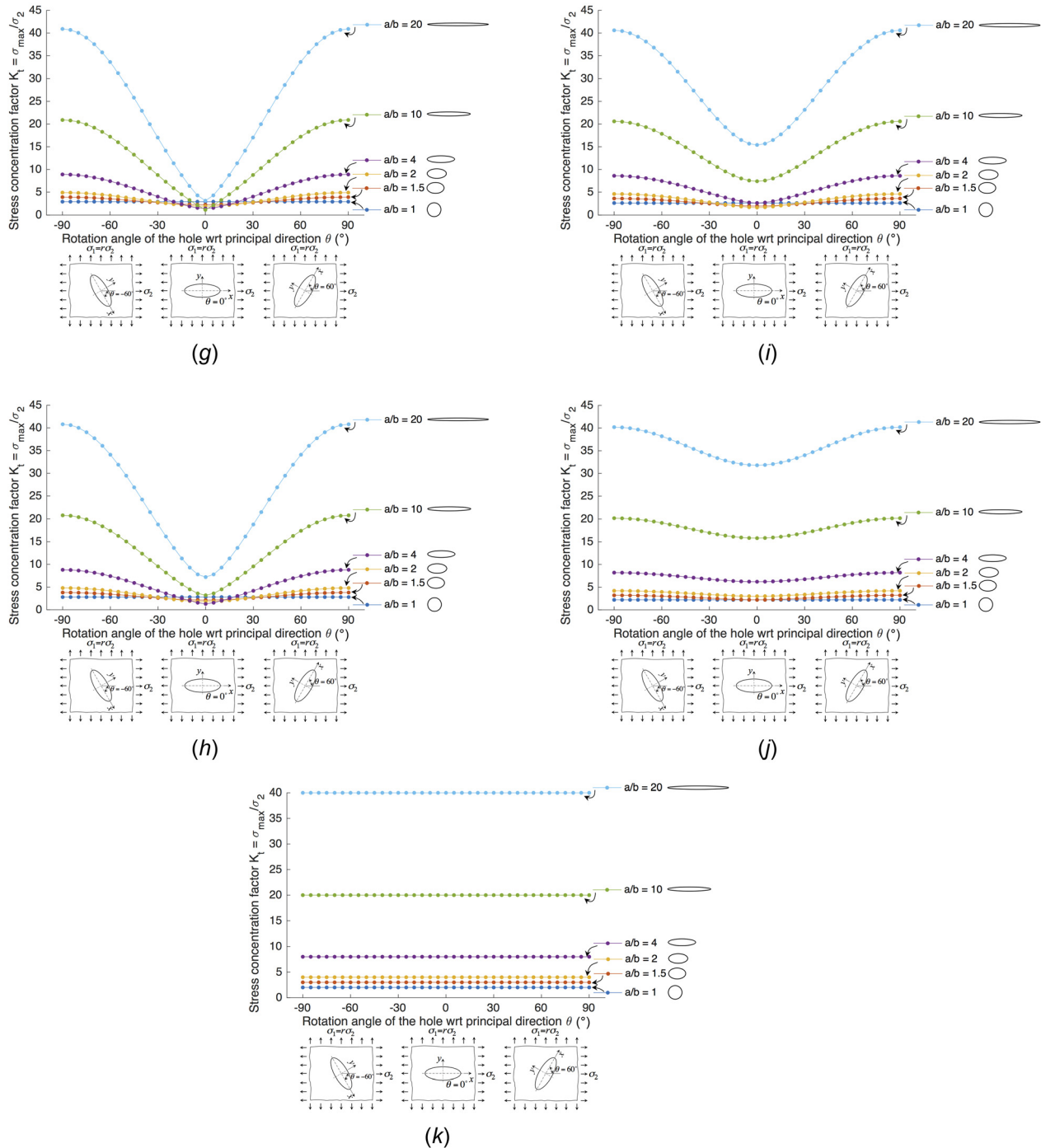


Fig. 4 (Continued)

angle θ that maximize stress with respect to the principal directions of an elliptical hole are difficult to formulate. Even for a specific value of a/b and r , with nonzero θ , the solution is still a convolute expression with inverse trigonometric functions. Here, we adopt a numeric strategy to handle Eq. (13) and visualize the impact of θ on the peak stress with the purpose of mitigating stress concentration.

Figure 4 shows that the stress concentration for $\sigma_1/\sigma_2 \geq 0$ is minimized by aligning the longitudinal axis of the elliptical hole to the principal direction, which corresponds to σ_2 , the larger principal stress. For $\sigma_1/\sigma_2 < 0$, there are exceptions since the stress concentration factor is determined as an absolute value, but the signs of the minimal stress and maximal stress may differ (some curves may have the lower portion mirrored upward).

However, if the effect of the aspect ratio is taken into account, it is still valid to state that the elliptical hole with the optimal aspect ratio should be aligned with the principal direction, which corresponds to σ_2 . The figure also shows that when the aspect ratio increases, the hole is more sensitive to rotation; a slight deviation from $\theta = 0$ results in a larger change of the stress concentration factor. Clearly, if a/b is 1, the circular hole is insensitive to rotation.

As a further note, the expression of stress distribution is significantly simplified for $\theta = 0$

$$(\sigma_\beta)_{\alpha_0} = \frac{(1+r)\sigma_2 \sin h 2\alpha_0 + (1-r)\sigma_2 [1 - e^{2\alpha_0} \cos 2\beta]}{\cos h 2\alpha_0 - \cos 2\beta} \quad (15)$$

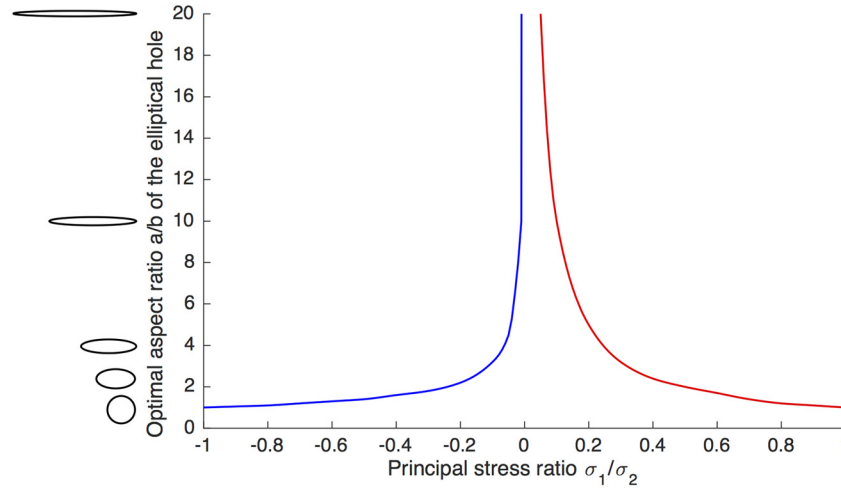


Fig. 5 Optimal aspect ratio of elliptical holes versus principal stress ratio σ_1/σ_2

Hence, possible locations for extreme values of $(\sigma_\beta)_{\alpha_0}$ can be found by setting the first-order derivative to zero

$$\frac{d(\sigma_\beta)_{\alpha_0}}{d\beta} = \frac{-2(re^{2\alpha_0} - e^{2\alpha_0} + r + 1)\sigma_2 \sin h2\alpha_0 \sin 2\beta}{(\cos h2\alpha_0 - \cos 2\beta)^2} = 0 \quad (16)$$

which shows that $(\sigma_\beta)_{\alpha_0}$ takes maximum or minimum at the tips of the hole ($\beta = 0$ or 0.5π).

3.2 Aspect Ratio of the Hole. To identify the optimal aspect ratio of the hole for a given stress ratio, we plot curves in Fig. 5, which illustrate the role of the aspect ratio as a function of the stress ratio. These results are in agreement with those found previously and indicate that hole alignment with the principal direction is the most favorable condition to reduce stress concentration.

Figure 5 shows the optimal aspect ratio of elliptical holes determined for each σ_1/σ_2 . The curve approaches an unbounded value when σ_1/σ_2 approaches zero from both sides. When $|\sigma_1/\sigma_2| = 1$, the circular hole is the best option. The y-axis of the plot is truncated at $a/b = 20$, for which K_t under uniaxial tension is 1.1. This value matches that obtained from existing expressions and design charts available in the classical literature [43,60]. Generally, the optimal aspect ratio decreases as $|\sigma_1/\sigma_2|$ increases from 0 to 1. However, the curve is not symmetric with the left half being steeper than the right one: for a given magnitude of $|\sigma_1/\sigma_2|$, the optimal a/b is smaller if σ_1/σ_2 is negative.

3.3 Application in Representative Volume Element and Role of Tessellation. The general observations in Secs. 3.1 and 3.2 are now applied to the RVE and the generic tessellations illustrated in Fig. 1 with the goal of elucidating how stress concentration develops in generic tessellations.

For any tessellation in Fig. 1 with tessellation angle ϕ and the ratio between displacement loadings $c = v/u$ (see Fig. 2), the principal stress ratio can be expressed as

$$r = \sigma_1/\sigma_2 = \frac{(1+\nu)(c + \sin \phi) - (1-\nu)\sqrt{c^2 - 2c \sin \phi + 1}}{(1+\nu)(c + \sin \phi) + (1-\nu)\sqrt{c^2 - 2c \sin \phi + 1}} \quad (17)$$

If the displacement loading is uniaxial, the principal stress ratio is

$$r = \sigma_1/\sigma_2 = \frac{1+\nu - \sqrt{\nu^2 + 2\nu + 1/\sin^2 \phi}}{1+\nu + \sqrt{\nu^2 + 2\nu + 1/\sin^2 \phi}} \quad (18)$$

With the principal stress ratio in Eq. (17) or Eq. (18), Fig. 4 or Fig. 5 can be used to determine the optimal aspect ratio and the minimum stress concentration factor corresponding to the displacement loading. Principal directions are determined using Eq. (8) or Eq. (10). As an illustrative example, the case of uniaxial tension in the horizontal direction is discussed in the following.

Using Eqs. (10) and (18), the principal direction and the principal stress ratio are determined and listed in Table 1. If the tessellation angle ϕ is 90 deg, the case is de facto uniaxial since σ_1 is 0. As ϕ decreases, the uniaxial displacement loading leads to non-zero shear strain (see Eq. (6)), nonzero σ_1 , and the principal direction of σ_2 is tilted away from the horizontal axis.

The impact of ϕ on stress concentration factors is illustrated in Fig. 6. The contour plots show values of the stress concentration factor in the RVE for uniaxial displacement loading in the horizontal direction where ϕ ranges from 10 deg to 90 deg. Table 1 lists the principal stress ratio at optimal γ (the absolute rotation angle measured from the positive X-direction) and a/b ; optimal layouts are also marked in the contour plots in Fig. 6. Clearly, when $\phi \neq 90$ deg, the uniaxial displacement creates shear strain in the RVE, and the principal stress field is not uniaxial. The effect is more pronounced as ϕ approaches zero. As a result, the principal direction is further away from horizontal and the optimal a/b gets smaller as the magnitude of σ_1/σ_2 increases. The stress concentration factor of the optimal shape also increases with increasing $|\sigma_1/\sigma_2|$ when ϕ approaches zero. The contour lines are symmetric

Table 1 Optimal absolute rotation angle and aspect ratio for elliptical holes in tessellated RVE under uniaxial tension

ϕ (deg)	10	20	30	40	50	60	70	80	90
σ_1/σ_2	-0.624	-0.388	-0.239	-0.143	-0.081	-0.042	-0.018	-0.004	0
Optimal γ (deg)	-38.31	-31.92	-26.03	-20.72	-15.93	-11.58	-7.54	-3.72	0
Optimal a/b	1.266	1.606	2.047	2.644	3.503	4.881	7.550	15.375	20.000
Min K_t	3.204	2.634	2.216	1.900	1.652	1.452	1.282	1.134	1.100

about the vertical line of optimal γ , but their shapes change from convex to concave when σ_1/σ_2 approaches -1 as ϕ reduces from 90 deg to 10 deg, in the same way as the evolution of the curves in Figs. 4(a)–4(f). As shown by the plots of optimal hole layouts in the RVE, the variation of ϕ can represent alternative tessellations, and even more complicated ones, e.g., Hexagonal and Kagome, can be realized by allowing multiple holes in the RVE.

Subplots in Fig. 7 depict the stress distributions of holes in multiple selected cases. The basic case of a circular hole with $\phi = 90$ deg in Fig. 7(a) shows that the maximum stress is $3.0\sigma_2$ at the vertical tip perpendicular to the horizontal loading and the stress at the

horizontal tip is $-1.0\sigma_2$ (the absolute value is plotted). If a/b increases, the stress at the horizontal tip is always $-1.0\sigma_2$, but the maximum stress reduces from $3.0\sigma_2$ to $2.0\sigma_2$ in Fig. 7(b) and $1.4\sigma_2$ in Fig. 7(c), always at the same location. The K_t of these three cases are precisely the results from Inglis's formula for elliptical holes under uniaxial tension [43,60]. In Figs. 7(d)–7(f), the tessellation angle and the aspect ratio are fixed at $\phi = 60$ deg and $a/b=5$, respectively, but the hole is rotated within the RVE. The stress distribution pattern in Fig. 7(d) is almost identical to that in Fig. 7(c) despite the change in ϕ , since the hole is also aligned with the principal direction (with $K_t=1.46$). If the hole is 10 deg from the

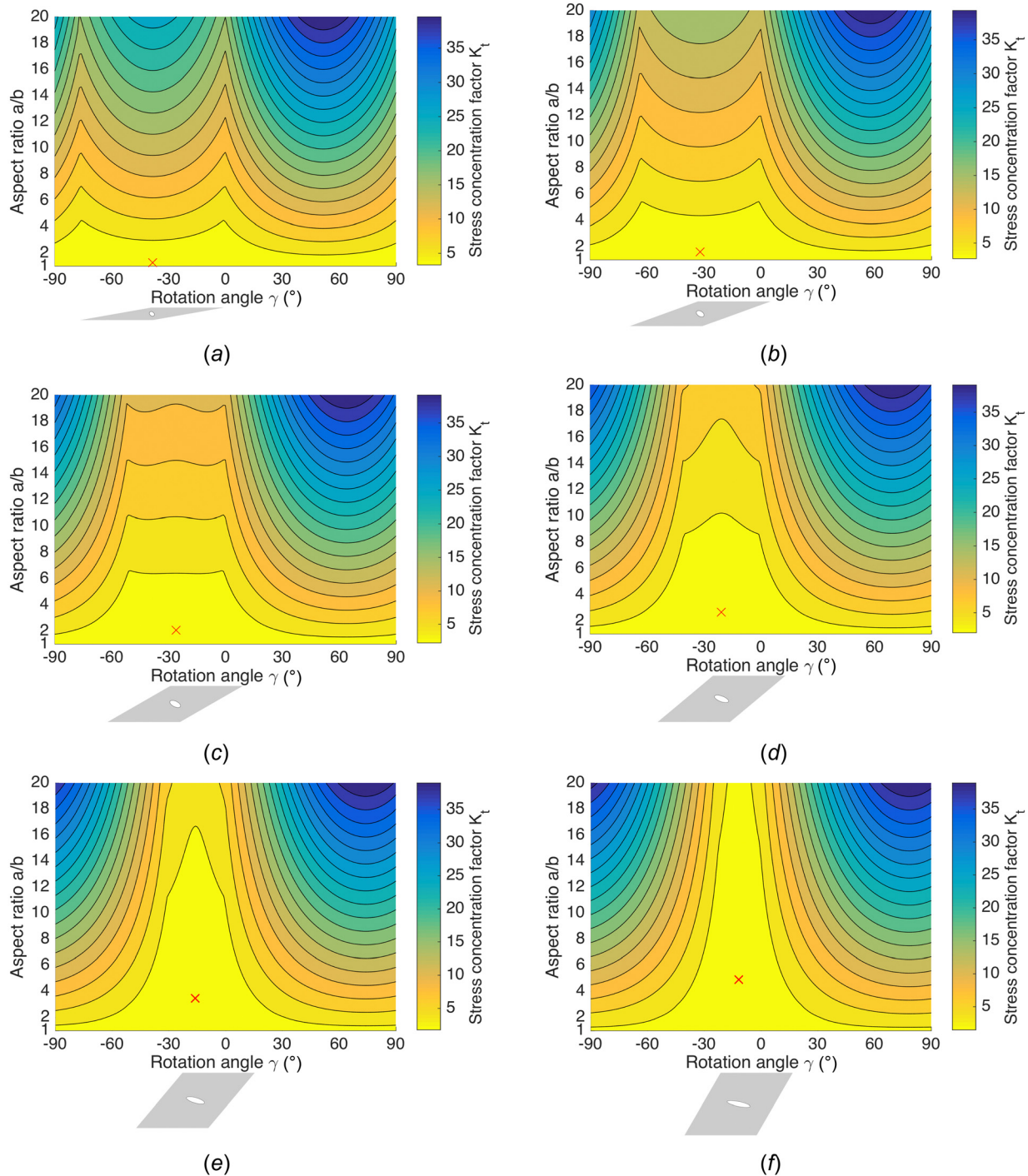


Fig. 6 Contour plots of stress concentration factor (K_t) as a function of aspect ratio and rotation angle of elliptical hole in the RVE, for tessellation angle from 10 deg to 90 deg, under uniaxial tension, with optimal hole layout marked and plotted: (a) $\phi = 10$ deg, (b) $\phi = 20$ deg, (c) $\phi = 30$ deg, (d) $\phi = 40$ deg, (e) $\phi = 50$ deg, (f) $\phi = 60$ deg, (g) $\phi = 70$ deg, (h) $\phi = 80$ deg, and (i) $\phi = 90$ deg

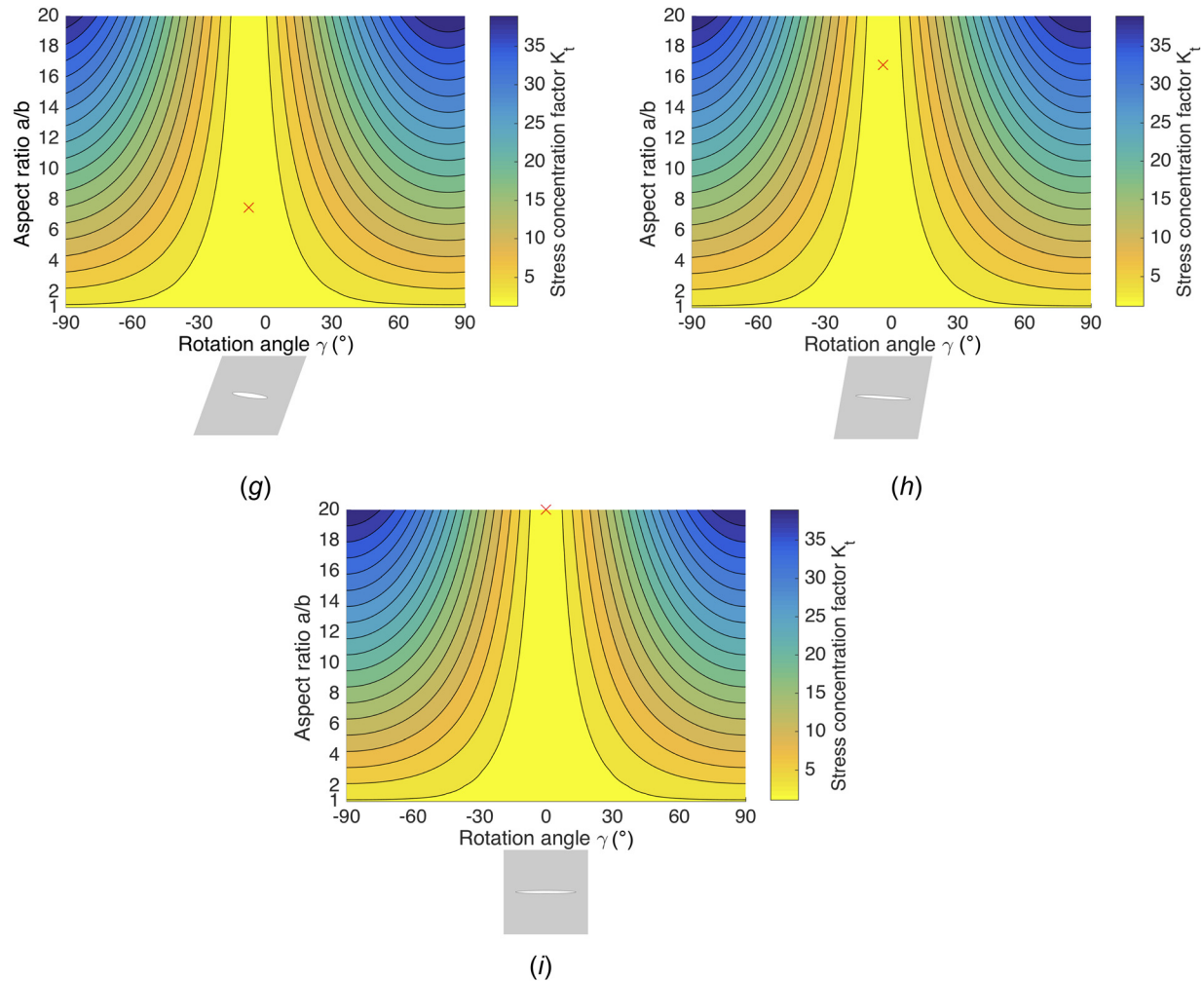


Fig. 6 (Continued)

principal direction, the peak stress no longer appears at the tip of the elliptical hole (K_t increases to 1.91), as shown in Fig. 7(e). If the hole is normal to the principal direction, K_t increases drastically to 11.04, at the location of the spikes in Fig. 7(f).

To study the effects of multiple holes, we consider the relative rotation between two identical holes. If two holes are far away from each other, their interaction can be ignored and the stress concentration factor is controlled by the worst case of the two. With this assumption, the contour plots of K_t as a function of γ and δ are generated and shown in Fig. 8. Three tessellation angles, $\phi = 30^\circ$, 60° , and 90° , are investigated with the aspect ratio selected as per Table 1. The contour plots again show the sensitivity of the stress concentration factor with respect to the rotation of holes and can be referenced to estimate K_t for architected planar materials with holes. The RVE plots illustrate that both holes in the RVE should be aligned with the principal direction for mitigating stress concentration. Such observation can be extended to tessellations with even more holes in the RVE, like Kagome.

4 Numerical Validation and Discussion

To check the validity of the theoretical model, we compare the theoretical prediction with finite element numerical studies using ABAQUS (Simulia, Providence, RI). A linear three-dimensional brick element with reduced integration (C3D8R) is adopted to model the RVE. After a convergence test, the number of elements is $\sim 15,000$ with local mesh refinement applied at the tips of each hole. For porosity $\psi = 0.25\%$, parametric studies with ϕ ranging from -90° to 90° and hole aspect ratio a/b taking a value

from the set (1, 2, 4, 10, 20) are performed for tessellation angle ϕ between 30° and 90° with 10° increment. If the RVE is solid, the displacement loading on the RVE ($L = 25$ mm) results in $\epsilon_{xx} = 7.0 \times 10^{-4}$ and $\epsilon_{yy} = 0.5\epsilon_{xx}$. The material is linear elastic with Young's modulus $E = 7.0 \times 10^4$ MPa and Poisson's ratio $\nu = 0.35$. Optimal values of γ and a/b can be determined by numerical optimization on the best shapes from parametric studies as implemented in MATLAB (MathWorks, Natick, MA).

The data in Table 2 demonstrate that the theoretical results match very well with those obtained numerically. The theoretical model successfully predicts the optimal value of rotation angle γ and aspect ratio a/b with less than 2% error for all ϕ . The predicted peak von Mises stress from the model is about 1% larger than numerical value. The difference in value is attributed to the use of bulk material properties for a fully solid RVE without reduction of porosity.

To check the porosity limits for the validity of our observation, we performed a number of finite element simulations of the rhombus RVE with hole aspect ratio $a/b = 2$ under uniaxial displacement loading in the X-direction with the goal of numerically determining the optimal θ to the nearest 1 deg.

The results tabulated in Table 3 show that for up to 5% porosity, the theoretical model predicts the orientation of the hole with less than 10% error. The theoretical prediction starts to deviate for porosity values larger than 10% and it fails for porosity equal or greater than 20%. If ψ is large, the hole is closer to the edge of RVE, defying the assumption of unbounded domain; hence, the problem cannot be treated by disregarding the hole size in the RVE and assuming bulk properties.

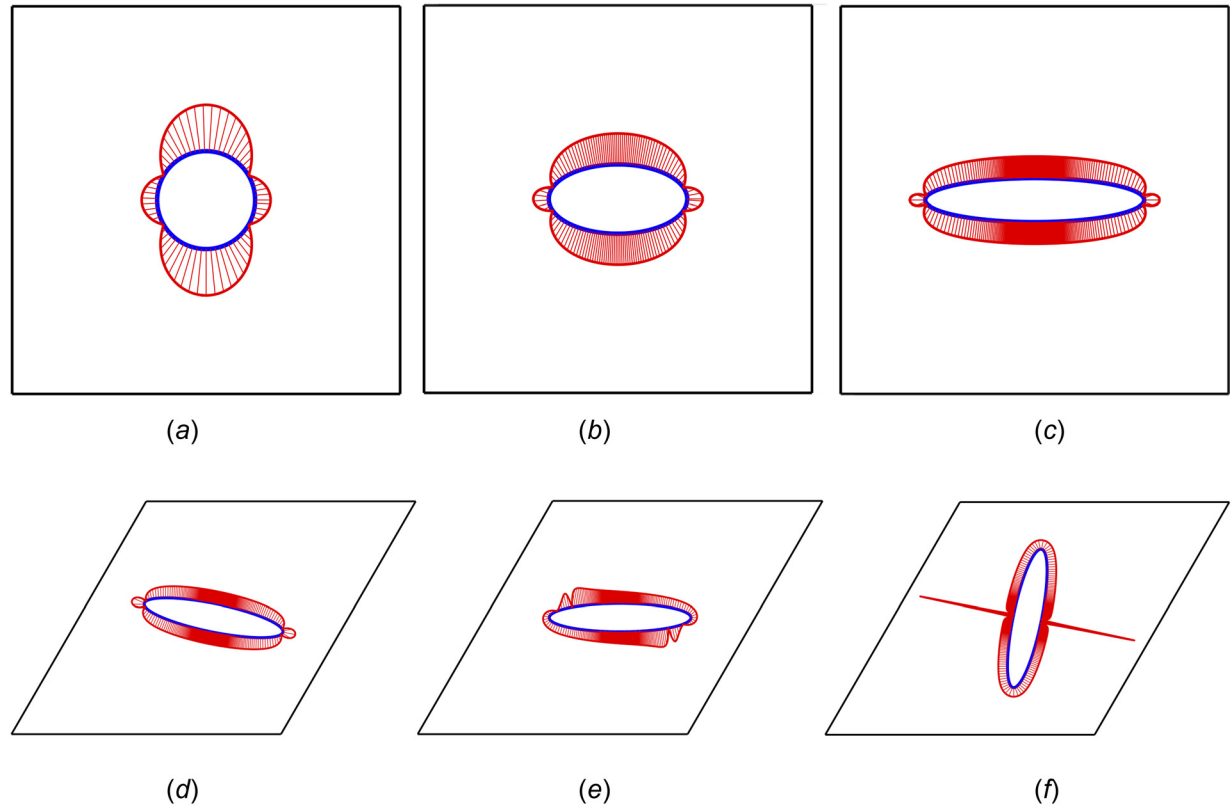


Fig. 7 Stress distribution plots of selected holes and tessellations under uniaxial loading: (a) $a/b = 1$, $\theta = 0$ deg, $\phi = 90$ deg, (b) $a/b = 2$, $\theta = 0$ deg, $\phi = 90$ deg, (c) $a/b = 5$, $\theta = 0$ deg, $\phi = 90$ deg, (d) $a/b = 5$, $\theta = 0$ deg, $\phi = 60$ deg, (e) $a/b = 5$, $\theta = 10$ deg, $\phi = 60$ deg, and (f) $a/b = 5$, $\theta = 90$ deg, $\phi = 60$ deg

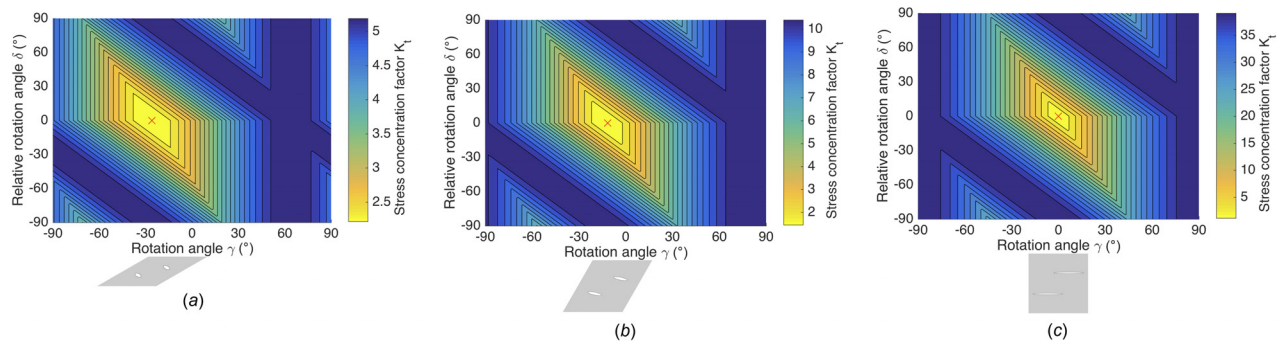


Fig. 8 Stress concentration factor (K_t) contour plots of absolute rotation γ and relative rotation δ for three tessellation angles, RVE under uniaxial tension, with optimal hole layout marked and plotted: (a) $a/b = 2$, $\phi = 30$ deg, (b) $a/b = 5$, $\phi = 60$ deg, and (c) $a/b = 20$, $\phi = 90$ deg

Table 2 Theoretical and numerical solutions of minimal peak von Mises stress under selected loading cases

ϕ (deg)	30	40	50	60	70	80	90
γ (deg), theory	−36.95	−33.62	−29.61	−24.55	−18.03	−9.71	0
γ (deg), numerical optimum	−36.90	−34.01	−29.78	−24.96	−17.99	−9.68	0
a/b , theory	3.64	2.44	1.92	1.63	1.49	1.40	1.38
a/b , numerical optimum	3.67	2.40	1.92	1.65	1.48	1.41	1.38
σ_{\max} (MPa), theory	114.09	114.47	113.95	114.04	114.07	113.46	113.27
σ_{\max} (MPa), numerical optimum	113.72	113.44	112.34	112.38	112.71	111.81	112.05

A set of finite element analyses of full-size samples with multiple holes was also performed. Figure 9(a) shows a model with 7×7 elliptical holes resembling the conditions of a periodic unbounded domain. After a convergence study, the model is meshed with $\sim 150,000$ C3D8R brick elements with local mesh

refinement at the tips of each hole. To approximate the boundary conditions in Eqs. (2) and (3) as applied in the RVE model (see Fig. 9(b)), translational displacements on the left edge and vertical displacement on the right edge are enforced. A uniaxial displacement load is applied on the right edge. The stress pattern on the

Table 3 Theoretical and numerical solutions of optimal hole rotation angle under uniaxial tension with multiple porosities

ϕ (deg)	30	40	50	60	70	80	90
γ (deg), theory	-26.03	-20.72	-15.93	-11.58	-7.54	-3.72	0
γ (deg), $\psi = 5\%$	-24	-20	-15	-10	-7	-3	0
γ (deg), $\psi = 7.5\%$	-22	-18	-14	-10	-6	-2	0
γ (deg), $\psi = 10\%$	-20	-16	-13	-6	-5	-2	0
γ (deg), $\psi = 15\%$	-13	-12	-7	-4	-1	0	0
γ (deg), $\psi = 20\%$	NA	-4	-1	1	3	1	0

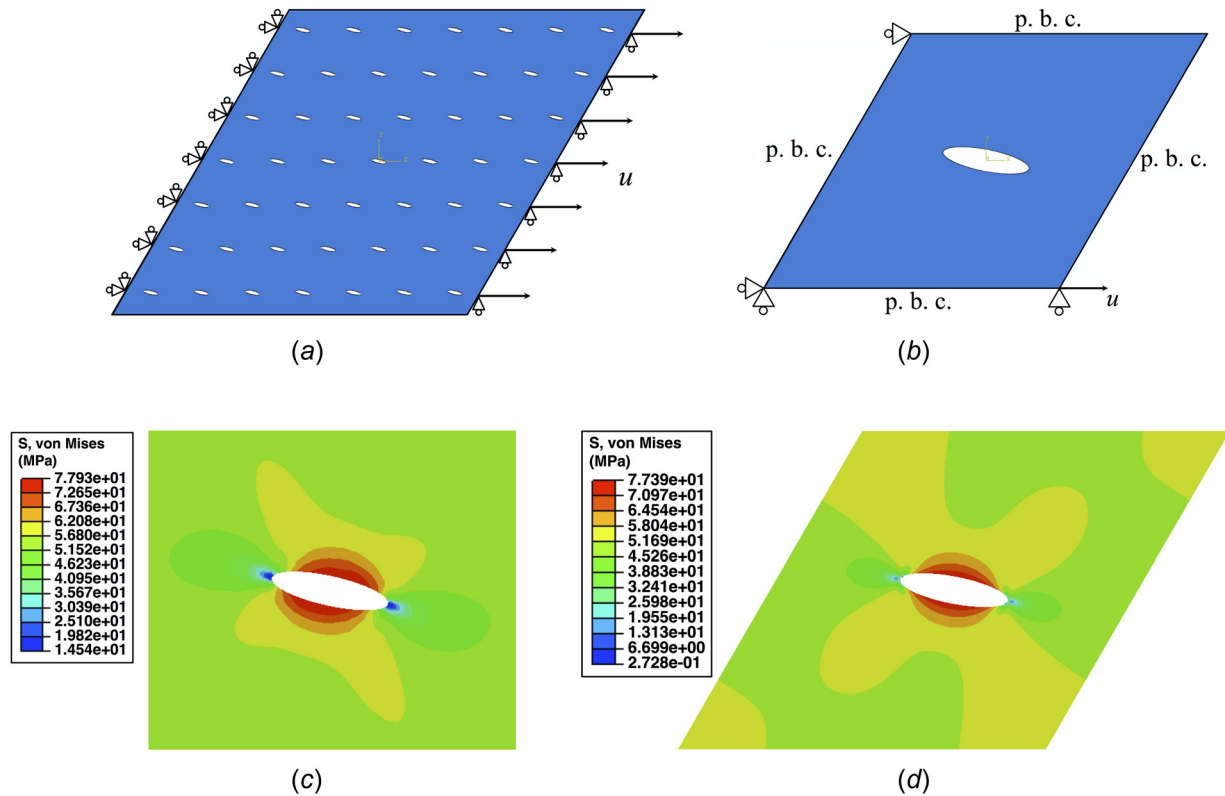


Fig. 9 Simulation results of full size versus RVE model with $a/b = 4$, $\theta = -12$ deg, $\phi = 60$ deg and $\psi = 2\%$: (a) Boundary conditions and loading of the full size model, (b) boundary conditions and loading of the RVE model, (c) von Mises stress distribution near the center hole of the full size model, and (d) von Mises stress distribution of the RVE model

edge of the center hole shown in Fig. 9(c) matches that of the single hole in the RVE model in Fig. 9(d) with only 1% difference in the von Mises stress. The orientation of the hole in Fig. 9(d) is the optimal value calculated from the theoretical model (Table 3), and the stress pattern is consistent with that in Fig. 7(d).

To complement the results in Fig. 8, which assume that the K_I is controlled by the worst of multiple holes, we numerically computed the minimum peak von Mises stress of elliptical holes with $a/b = 5$ in triangular, hexagonal, and Kagome tessellation under uniaxial displacement with porosity up to 5%. The selected tessellations correspond to $\phi = 60$ deg with 1, 2, and 3 holes in the RVE, as shown in Figs. 1(c) and 8(b). Results in a given row of

Table 4 Numerical solutions of minimal peak von Mises stress of elliptical holes in triangular, hexagonal, and Kagome tessellations under uniaxial tension

Tessellation	Triangular	Hexagonal	Kagome
σ_{\max} (MPa), $\psi = 1\%$	73.75	74.27	75.80
σ_{\max} (MPa), $\psi = 2\%$	74.12	77.74	78.33
σ_{\max} (MPa), $\psi = 5\%$	75.01	91.21	86.67

Table 4 show the peak stress increases by less than 20% as more holes are introduced, suggesting the minimum peak stress is less sensitive to the number of holes if the porosity is low and the holes are far apart. This shows that the observations on the optimal orientation and aspect ratio of elliptical holes for mitigation of stress concentration are valid for a wide range of generic planar tessellations.

The insights gained in this paper can assist engineers to retrieve the optimal parameters of elliptical holes for a given loading and tessellation angle, as well as to predict the peak stress of one single hole with relatively good accuracy. The results also enable the stress prediction for generic tessellation of planar patterns of a finite number of separated holes. While the minimum distance between holes to be considered as uninfluential to the neighboring holes behavior cannot be prescribed precisely for a general problem, relevant guidelines can be found in the literature [43]. The theoretical model and the outcome of minimizing stress by aligning the hole to the principle stress direction of rhombus shaped RVEs can be extended to parallelograms by changing the edge lengths. Extension of the model and inclusions to other polygonal RVE shapes is also expected to be valid but further work is required. This work focuses on stress prediction of tessellated elliptical holes in a linear elastic material with porosity below 5%.

Further work is required to develop theoretical predictions that accounts for damage, plastic failure, and other physical phenomena.

5 Conclusions

In this paper, generic planar tessellations of elliptical holes with varying orientations in a low-porosity domain under biaxial displacement loading have been investigated with the goal of mitigating stress concentration. The proposed theoretical model predicts stress distribution on the edge of the hole and shows that the alignment of the hole with the principal direction corresponding to the largest principal stress is the key to minimizing stress concentration. The optimal aspect ratio of the elliptical hole has been identified for various load cases: circular holes are optimal for equiaxial stress and increasingly large aspect ratio holes for stress state approaching uniaxial. Numerical simulations of generic rhombus shaped RVE have demonstrated the validity of the theoretical model for porosity up to 5% and for representation of arbitrary planar tessellations with a finite number of separated holes. The theoretical model and findings presented address the crucial issue of stress concentration and can be applied to the design of planar architected materials for mechanical, aerospace, biomedical, and other engineering applications.

Acknowledgment

Any opinions, findings, and conclusions or recommendations expressed in this publication are those of the authors and do not necessarily reflect the views of Siemens and NSERC.

Funding Data

- Natural Sciences and Engineering Research Council of Canada (Grant Nos. 242363 and 242561).

References

- [1] Ashby, M., and Bréchet, Y., 2003, "Designing Hybrid Materials," *Acta Mater.*, **51**(19), pp. 5801–5821.
- [2] Lee, M. G., Lee, J. W., Han, S. C., and Kang, K., 2016, "Mechanical Analyses of 'Shellular', an Ultralow-Density Material," *Acta Mater.*, **103**, pp. 595–607.
- [3] Zheng, X., Smith, W., Jackson, J., Moran, B., Cui, H., Chen, D., Ye, J., Fang, N., Rodriguez, N., and Weisgraber, T., 2016, "Multiscale Metallic Metamaterials," *Nat. Mater.*, **15**(10), p. 1100.
- [4] Elsayed, M. S., and Pasini, D., 2010, "Analysis of the Elastostatic Specific Stiffness of 2D Stretching-Dominated Lattice Materials," *Mech. Mater.*, **42**(7), pp. 709–725.
- [5] Abad, E. M. K., Khanoki, S. A., and Pasini, D., 2013, "Fatigue Design of Lattice Materials Via Computational Mechanics: Application to Lattices With Smooth Transitions in Cell Geometry," *Int. J. Fatigue*, **47**, pp. 126–136.
- [6] Wang, Z., Jing, L., Ning, J., and Zhao, L., 2011, "The Structural Response of Clamped Sandwich Beams Subjected to Impact Loading," *Compos. Struct.*, **93**(4), pp. 1300–1308.
- [7] Grima, J. N., and Gatt, R., 2010, "Perforated Sheets Exhibiting Negative Poisson's Ratios," *Adv. Eng. Mater.*, **12**(6), pp. 460–464.
- [8] Bertoldi, K., Reis, P. M., Willshaw, S., and Mullin, T., 2010, "Negative Poisson's Ratio Behavior Induced by an Elastic Instability," *Adv. Mater.*, **22**(3), pp. 361–366.
- [9] Mitschke, H., Schwerdtfeger, J., Schury, F., Stingl, M., Körner, C., Singer, R. F., Robins, V., Mecke, K., and Schröder-Turk, G. E., 2011, "Finding Auxetic Frameworks in Periodic Tessellations," *Adv. Mater.*, **23**(22–23), pp. 2669–2674.
- [10] Overvelde, J. T. B., Shan, S., and Bertoldi, K., 2012, "Compaction Through Buckling in 2D Periodic, Soft and Porous Structures: Effect of Pore Shape," *Adv. Mater.*, **24**(17), pp. 2337–2342.
- [11] Shim, J., Shan, S., Košmrlj, A., Kang, S. H., Chen, E. R., Weaver, J. C., and Bertoldi, K., 2013, "Harnessing Instabilities for Design of Soft Reconfigurable Auxetic/Chiral Materials," *Soft Matter*, **9**(34), pp. 8198–8202.
- [12] Shan, S., Kang, S. H., Zhao, Z., Fang, L., and Bertoldi, K., 2015, "Design of Planar Isotropic Negative Poisson's Ratio Structures," *Extreme Mech. Lett.*, **4**, pp. 96–102.
- [13] Gatt, R., Mizzi, L., Azzopardi, J. I., Azzopardi, K. M., Attard, D., Casha, A., Briffa, J., and Grima, J. N., 2015, "Hierarchical Auxetic Mechanical Metamaterials," *Sci. Rep.*, **5** (1), p. 8395.
- [14] Carta, G., Brun, M., and Baldi, A., 2016, "Design of a Porous Material With Isotropic Negative Poisson's Ratio," *Mech. Mater.*, **97**, pp. 67–75.
- [15] Liu, J., Gu, T., Shan, S., Kang, S. H., Weaver, J. C., and Bertoldi, K., 2016, "Harnessing Buckling to Design Architected Materials That Exhibit Effective Negative Swelling," *Adv. Mater.*, **28**(31), pp. 6619–6624.
- [16] Mullin, T., Deschanel, S., Bertoldi, K., and Boyce, M. C., 2007, "Pattern Transformation Triggered by Deformation," *Phys. Rev. Lett.*, **99**(8), p. 084301.
- [17] Bertoldi, K., Boyce, M. C., Deschanel, S., Prange, S., and Mullin, T., 2008, "Mechanics of Deformation-Triggered Pattern Transformations and Superelastic Behavior in Periodic Elastomeric Structures," *J. Mech. Phys. Solids*, **56**(8), pp. 2642–2668.
- [18] Bertoldi, K., and Boyce, M., 2008, "Mechanically Triggered Transformations of Phononic Band Gaps in Periodic Elastomeric Structures," *Phys. Rev. B*, **77**(5), p. 052105.
- [19] Bertoldi, K., and Boyce, M. C., 2008, "Wave Propagation and Instabilities in Monolithic and Periodically Structured Elastomeric Materials Undergoing Large Deformations," *Phys. Rev. B*, **78**(18), p. 184107.
- [20] Tang, Y., Lin, G., Han, L., Qiu, S., Yang, S., and Yin, J., 2015, "Design of Hierarchically Cut Hinges for Highly Stretchable and Reconfigurable Metamaterials With Enhanced Strength," *Adv. Mater.*, **27**(44), pp. 7181–7190.
- [21] Lu, T., Stone, H., and Ashby, M., 1998, "Heat Transfer in Open-Cell Metal Foams," *Acta Mater.*, **46**(10), pp. 3619–3635.
- [22] Lakes, R., 1996, "Cellular Solid Structures With Unbounded Thermal Expansion," *J. Mater. Sci. Lett.*, **15**(6), pp. 475–477.
- [23] Lehman, J., and Lakes, R., 2013, "Stiff Lattices With Zero Thermal Expansion and Enhanced Stiffness Via Rib Cross Section Optimization," *Int. J. Mech. Mater. Des.*, **9**(3), pp. 213–225.
- [24] Lehman, J., and Lakes, R., 2013, "Stiff, Strong Zero Thermal Expansion Lattices Via the Poisson Effect," *J. Mater. Res.*, **28**(17), pp. 2499–2508.
- [25] Lehman, J., and Lakes, R. S., 2014, "Stiff, Strong, Zero Thermal Expansion Lattices Via Material Hierarchy," *Compos. Struct.*, **107**, pp. 654–663.
- [26] Xu, H., and Pasini, D., 2016, "Structurally Efficient Three-Dimensional Metamaterials With Controllable Thermal Expansion," *Sci. Rep.*, **6**(1), p. 34924.
- [27] Xu, H., Farag, A., and Pasini, D., 2017, "Multilevel Hierarchy in Bi-Material Lattices With High Specific Stiffness and Unbounded Thermal Expansion," *Acta Mater.*, **134**, pp. 155–166.
- [28] Khanoki, S. A., and Pasini, D., 2012, "Multiscale Design and Multiobjective Optimization of Orthopedic Hip Implants With Functionally Graded Cellular Material," *ASME J. Biomech. Eng.*, **134**(3), p. 031004.
- [29] Arabnejad, S., Johnston, B., Tanzer, M., and Pasini, D., 2017, "Fully Porous 3D Printed Titanium Femoral Stem to Reduce Stress-Shielding Following Total Hip Arthroplasty," *J. Orthop. Res.*, **35**(8), pp. 1774–1783.
- [30] Rahimizadeh, A., Nourmohammadi, Z., Arabnejad, S., Tanzer, M., and Pasini, D., 2018, "Porous Architected Biomaterial for a Tibial-Knee Implant With Minimum Bone Resorption and Bone-Implant Interface Micromotion," *J. Mech. Behav. Biomed. Mater.*, **78**, pp. 465–479.
- [31] Abad, E. M. K., Pasini, D., and Cecere, R., 2012, "Shape Optimization of Stress Concentration-Free Lattice for Self-Expandable Nitinol Stent-Grafts," *J. Biomech.*, **45**(6), pp. 1028–1035.
- [32] Lakes, R., 1993, "Materials With Structural Hierarchy," *Nature*, **361**(6412), p. 511.
- [33] Cho, Y., Shin, J.-H., Costa, A., Kim, T. A., Kunin, V., Li, J., Lee, S. Y., Yang, S., Han, H. N., and Choi, I.-S., 2014, "Engineering the Shape and Structure of Materials by Fractal Cut," *Proc. Natl. Acad. Sci. U.S.A.*, **111**(49), pp. 17390–17395.
- [34] Overvelde, J. T., Weaver, J. C., Hoberman, C., and Bertoldi, K., 2017, "Rational Design of Reconfigurable Prismatic Architected Materials," *Nature*, **541**(7637), p. 347.
- [35] Sigmund, O., and Torquato, S., 1999, "Design of Smart Composite Materials Using Topology Optimization," *Smart Mater. Struct.*, **8**(3), p. 365.
- [36] Taylor, M., Francesconi, L., Gerendás, M., Shanian, A., Carson, C., and Bertoldi, K., 2014, "Low Porosity Metallic Periodic Structures With Negative Poisson's Ratio," *Adv. Mater.*, **26**(15), pp. 2365–2370.
- [37] Javid, F., Wang, P., Shanian, A., and Bertoldi, K., 2016, "Architected Materials With Ultra-Low Porosity for Vibration Control," *Adv. Mater.*, **28**(28), pp. 5943–5948.
- [38] Javid, F., Liu, J., Rafsanjani, A., Schaezner, M., Pham, M. Q., Backman, D., Yandt, S., Innes, M. C., Booth-Morrison, C., and Gerendas, M., 2017, "On the Design of Porous Structures With Enhanced Fatigue Life," *Extreme Mech. Lett.*, **16**, pp. 13–17.
- [39] Grima, J. N., Mizzi, L., Azzopardi, K. M., and Gatt, R., 2016, "Auxetic Perforated Mechanical Metamaterials With Randomly Oriented Cuts," *Adv. Mater.*, **28**(2), pp. 385–389.
- [40] Rafsanjani, A., Akbarzadeh, A., and Pasini, D., 2015, "Snapping Mechanical Metamaterials Under Tension," *Adv. Mater.*, **27**(39), pp. 5931–5935.
- [41] Rafsanjani, A., and Bertoldi, K., 2017, "Buckling-Induced Kirigami," *Phys. Rev. Lett.*, **118**(8), p. 084301.
- [42] Timoshenko, S., and Goodier, J., 1970, *Theory of Elasticity*, McGraw-Hill, New York.
- [43] Pilkey, W. D., and Pilkey, D. F., 2008, *Peterson's Stress Concentration Factors*, Wiley, Hoboken, NJ.
- [44] Durelli, A., Parks, V., and Feng, H., 1966, "Stresses Around an Elliptical Hole in a Finite Plate Subjected to Axial Loading," *ASME J. Appl. Mech.*, **33**(1), pp. 192–195.
- [45] Kassir, M., and Sih, G. C., 1966, "Three-Dimensional Stress Distribution Around an Elliptical Crack Under Arbitrary Loadings," *ASME J. Appl. Mech.*, **33**(3), pp. 601–611.

- [46] Givoli, D., and Elishakoff, I., 1992, "Stress Concentration at a Nearly Circular Hole With Uncertain Irregularities," *ASME J. Appl. Mech.*, **59**(2S), pp. S65–S71.
- [47] Shivakumar, K., and Newman, J., 1995, "Stress Concentration Equations for Straight-Shank and Countersunk Holes in Plates," *ASME J. Appl. Mech.*, **62**(1), pp. 248–249.
- [48] Murthy, M. V., 1969, "Stresses Around an Elliptic Hole in a Cylindrical Shell," *ASME J. Appl. Mech.*, **36**(1), pp. 39–46.
- [49] Youngdahl, C. K., and Sternberg, E., 1966, "Three-Dimensional Stress Concentration Around a Cylindrical Hole in a Semi-Infinite Elastic Body," *ASME J. Appl. Mech.*, **33**(4), pp. 855–865.
- [50] Lee, E. J., and Klang, E. C., 1992, "Stress Distribution in an Edge-Stiffened Semi-Infinite Elastic Plate Containing a Circular Hole," *ASME J. Appl. Mech.*, **59**(4), pp. 789–795.
- [51] Chau, K., and Wei, X., 2001, "Stress Concentration Reduction at a Reinforced Hole Loaded by a Bonded Circular Inclusion," *ASME J. Appl. Mech.*, **68**(3), pp. 405–411.
- [52] Seide, P., and Hafiz, A., 1975, "Stress Concentration in a Stretched Cylindrical Shell With Two Equal Circular Holes," *ASME J. Appl. Mech.*, **42**(1), pp. 105–109.
- [53] Hansen, E. B., 1978, "Stress Concentration in a Stretched Cylindrical Shell With Two Elliptical Holes," *ASME J. Appl. Mech.*, **45**(4), pp. 839–844.
- [54] Chen, W. T., 1970, "Stress Concentration Around Spheroidal Inclusions and Cavities in a Transversely Isotropic Material Under Pure Shear," *ASME J. Appl. Mech.*, **37**(1), pp. 85–92.
- [55] Atsumi, A., and Itou, S., 1973, "Stresses in a Transversely Isotropic Slab Having a Spherical Cavity," *ASME J. Appl. Mech.*, **40**(3), pp. 752–758.
- [56] Hwu, C., 1990, "Anisotropic Plates With Various Openings Under Uniform Loading or Pure Bending," *ASME J. Appl. Mech.*, **57**(3), pp. 700–706.
- [57] Attar, M. M., 2013, "Analytical Study of Two Pin-Loaded Holes in Unidirectional Fiber-Reinforced Composites," *ASME J. Appl. Mech.*, **80**(2), p. 021004.
- [58] Rao, M. B., and Murthy, M., 1977, "Stress Concentration Around an Elliptic Hole in a Cylindrical Shell Under Torsion With Major Axis of the Hole Perpendicular to the Shell Axis," *ASME J. Appl. Mech.*, **4**(1), pp. 184–186.
- [59] Shilkrut, D., and Ben-Gad, E., 1985, "Elastic Stress Concentration Phenomena in an Axially Stressed Rectangular Plate With a Central Circular Hole and Other Related Problems," *ASME J. Appl. Mech.*, **52**(1), pp. 216–219.
- [60] Inglis, C. E., 1913, "Stresses in a Plate Due to the Presence of Cracks and Sharp Corners," *Trans. R. Inst. Nav. Archit.*, **55**(219–241), pp. 193–198.